Micro-PIV visualization and numerical simulation of flow and heat transfer in three micro pin-fin heat sinks

XIA, Guodong, CHEN, Zhuo, CHENG, Lixin, MA, Dandan, ZHAI, Yuling and YANG, Yuchen

Published version

XIA, Guodong, CHEN, Zhuo, CHENG, Lixin, MA, Dandan, ZHAI, Yuling and YANG, Yuchen (2017). Micro-PIV visualization and numerical simulation of flow and heat transfer in three micro pin-fin heat sinks. International Journal of Thermal Sciences, 119, 9-23.

Micro-PIV visualization and numerical simulation of flow and heat transfer in three micro pin-fin heat sinks

Guodong Xia[*a], Zhuo Chen [a], Lixin Cheng[*a,b], Dandan Ma [a], Yuling Zhai[a] and Yuchen Yang [a]

[a]*College of Environmental and Energy Engineering, Beijing University of Technology, Beijing, 100124, P. R. China*

[b]*Department of Engineering and Mathematics, Faculty of Arts, Computing, Engineering and Science, Sheffield Hallam University, City Campus, Howard Street, Sheffield S1 1WB, UK*

Abstract

This paper presents the experimental results of laminar flow behavior of water in circular micro pin-fin (C-MPF), square micro pin-fin (S-MPF) and diamond micro pin-fin (D-MPF) heat sinks using micro-PIV flow visualization technology at first. All three micro pin-fin heat sinks have a hydraulic diameter of 200 μm. Second, numerical simulation results of the fluid flow characteristics in these heat sinks with CFD are compared to the experimental results of fluid flow behaviors measured with the micro-PIV flow visualization. The normalized time averaged streamline patterns and instantaneous velocity contours in the three heat sinks were obtained for laminar flow of Reynolds number from 10 to 200. By comparison, the

[*] Corresponding authors, email: xgd@bjut.edu.cn; lixincheng@hotmail.com

experimental results favorably agree with the simulated results of fluid flow. Of the three types of heat sinks, the vortexes occur the earliest in the D-MPF heat sink, which also present very complicated back flow. The strong vortexes and back flow effectively enhance the mixing of fluid and therefore lead to higher pressure drops in the D-MPF heat sink as compared to the other two types of heat sinks. The vortexes in the D-MPF heat sink are very much easily involved in the main flow than those in the other two types of heat sinks due to the high deceleration and pressurization zone. Finally, numerical simulation results of heat transfer at steady state in the three heat sinks are presented. The initial temperature of the working fluid and the ambient air is maintained at 293 K and a constant heat flux of q_w = 400 kW/m^2 is adopted in the central area at the bottom of the heat sink. The Reynolds number ranges from 40 to 300 for the fluid flow and heat transfer simulations. It shows that D-MPF heat sink has better heat transfer performance than the other two type heat sinks. The combined effects of the vortex in the main flow at the front side wall and the strong vortex intensity behind the D-MPF heat sink obtained in both experimental and numerical results may reasonably explain the better heat transfer enhancement behaviors as compared to those in the other two types of heat sinks. Further experiments on the heat transfer performance will be conducted to compare to the simulated results in the follow-up planned research.

Key words: Micro-PIV; experiment; micro pin-fin; laminar flow; velocity field; vortex; heat transfer; pressure drop; numerical simulation; heat transfer enhancement.

1. Introduction

Applications of microscale thermal and fluid flow phenomena in various micro devices and systems, micro-cooling technology in the computer and electronics industries, MEMS(Micro-Electro-Mechanical-Systems), NEMS(Nano-Electro-Mechanical-Systems), energy, power, renewable energy, mechanical, aerospace, process, biological and chemical engineering, and relevant interdisciplinary subjects etc. have received considerable attention in recent years [1-8]. With the rapid development of large scale integrated circuit, the cooling demand of microelectronic chip per unit area is as high as 10^7 W/m^2 [9], an effective and reliable method is urgently needed to solve the problem of high flux removal with effective methods. Micro heat sinks using both single phase and two phase cooling become one of the most promising and efficient cooling methods [1-8]. Single phase flow cooling is still widely used with developing various new structures such as pin fin heat sinks to enhance heat transfer behaviors. It is thus important to understand the fluid flow and heat transfer characteristics in micro-pin fin heat sinks with various structures, especially utilizing state-of-the-art micro-PIV visualization technology and numerical simulation methods to understand the fluid flow and heat transfer behaviors.

Tuckerman and Pease [1, 7] were the first to introduce the concept of microchannels and evaluate the performance of micro-pin fins which were arranged in an in-line pattern. Since then, fluid flow and heat transfer in micro-pin fin heat sinks with new structures have been extensively investigated over the past years. Peles et al. [8] investigated heat transfer and pressure drop phenomena over a bank of micro-pin fins. A simplified expression for the total

thermal resistance has been derived analytically and validated experimentally, which geometrical and thermo-hydraulic parameters affecting are considered. Kosar and Peles [10] performed an experimental study on heat transfer and pressure drop of de-ionized water over a bank of shrouded staggered micro pin fins 243μm long with hydraulic diameter of 99.5 μm. They suggested that a comprehensive design should be undertaken to develop heat sinks containing pin fin geometrical configurations which significantly reduce the pressure drop while maintaining superior heat transfer characteristics. Kosar and Peles [11] performed a parametric study of heat transfer and pressure drop associated with forced flow of deionized water over five micro-pin fin heat sinks of different spacing, arrangements, and shapes experimentally. Their results indicated that utilizing streamlined pin fin heat sinks may significantly enhance the thermal-hydraulic performance of the heat sink, but only at moderate Reynolds number range. Experimental results of the thermal and hydraulic performances of silicon-based, low aspect ratio micro-pin fin cold plates under cross flow conditions was reported by Prasher et al. [12]. It was found that the average Nusselt number and friction factor varied with the Reynolds number and flow visualization studies might be needed to understand the transition in the behavior of friction factor for low Reynolds number around 100 for water. Jeng et al. [13] analyzed the pressure drop and heat transfer of square pin-fin arrays with variable longitudinal and transverse pitch in in-line and staggered arrangements using the transient single-blow technique. The entropy minimization method was applied to optimize the heat sink with staggered arrays of pin fin and tip clearance by Shi et al. [14]. It was found that the effect of tip clearance was more pronounced for conductive at the high aspect ratio, compared with convective, while the convective effect dominated at low

ratio. Xia et al [15] investigated experimentally and numerically the temperature distribution and pressure drop behavior to interpret the complex thermal behavior and flow field in the very complex corrugation of microchannel heat sink. They observed that the vortex became bigger and moved to the middle of the channel with increasing of flow rate. The heat transfer enhancement mechanisms can be attributed to the heat transfer area enlarged, thermal boundary interrupted and redeveloped, chaotic advection, hot and cooling fluid better mixed by vortex formed in the reentrant cavity. The second flow and recirculation flow motions in bifurcations and bends in symmetric fractal-like microchannel networks with two branching levels were studied through three-dimensional simulations by Zhang et al. [16]. The effects of Reynolds number and aspect ratio on the vortices generation were compared. It showed that the fractal-like microchannel network with a smaller aspect ratio of 0.333 had the lowest pressure drop and highest heat transfer performance. Zhao et al. [17] proposed a geometry optimizing method changing pin-fin porosity and pin-fin located angle. They numerically studied the effects of porosity and located angle of the micro square pin-fin heat sink and found that the optimal porosity and located angle for thermal performance were 0.75 and 30° respectively. Furthermore, compared to the circular pin fin heat sink, micro heat sinks with the optimized square pin fin presented better thermal performance. Izci et al. [18] numerically studied micro pin-fins with different shapes but the same chord thickness/diameter. Their results indicated that the rectangular-shaped micro pin-fin has the highest Nusselt number and friction factor over the same Reynolds number, while the cone-shaped micro pin-fin has the best thermal performance index, which meant that micro pin-fins with unconventional shapes could be more preferable in micro pin-fin heat sinks. Renfer et al. [19] experimentally

investigated the effect of vortex shedding to the heat transfer enhancement. After factoring in the rise in pumping power, yields local Nusselt number increases up to 190% due to the vortex-induced fluctuations and mixing, which also induced a pressure drop increase. By using micron-resolution laser-induced fluorescence (μLIF), the vortex shedding was confirmed to be the reason for both the elimination of liquid hotspots and the exceptional augmentation in heat transfer.

From the foregoing literature review, it is evident that many experimental and numerical studies on the fluid flow and heat transfer in various micro heat sinks have been conducted over the past years. As a different type of micro heat sinks, micro-pin fin heat sinks have presented a promising opportunity to improve the heat transfer performance through optimizing the structure along with more complicated thermal behaviors and flow field. However, experimental studies on the micro scale flow in the micro heat sinks are very limited due to the technical difficulties. Therefore, it is of great significance to study the flow fields using innovative micro-PIV flow visualization technology to understand the very complex fluid flow phenomena involved, which may be helpful to explain the mechanisms of heat transfer enhancement.

Micro-Particle Image Velocimetry (Micro-PIV) technique is one of the best techniques for an accurate determination of steady state velocity profiles for liquid flows in microchannels as performed by Sinton [20]. Combining laser with image processing technology, the micro-PIV was applied to measure instantaneous and ensemble-averaged flow fields in microfluidic systems by Santiago et al. [21]. The velocity vector fields were measured with spatial resolutions down to 6.9×6.9 μm^2. The Hele-Shaw flow field around a

30 μm elliptical cylindrical obstruction in the center of a 120 μm square cross-section channel was studied, with a bulk velocity of approximately 50 μm/s. Micro-PIV has become the most promising visualization technique to study the flow field. Meinhart et al. [22] demonstrated the accuracy of the micro-PIV system by measuring the known flow field in a 30 × 300 μm^2 glass microchannel with a spatial resolution of 6.9 × 6.9 μm^2. Silva et al. [23] employed the micro-PIV to determine geometric parameters of the microchannels. Their results have demonstrated that the accuracy is 10 times higher than that of a conventional optical microscope, and the accuracy of the micro-PIV results has been validated. Jung et al. [24] studied the flow field around a micropillar confined in a microchannel using micro-PIV technology. The flow parameters such as flow field, spanwise vorticity, and turbulent kinetic energy are quantified and the flow regimes of cylinder-diameter-based Reynolds number at 100 to700 (i.e., steady, transition from quasi-steady to unsteady, and unsteady flow) were elucidated. Renfer et al. [25] investigated the hydrodynamics in microcavities with cylindrical micro-pin fin arrays including inline and staggered pin arrangements by means of pressure drop and micro-PIV measurements. The post-transition flow field showed vortex shedding and flow impingement onto the pins explaining the pressure drop increase. Yu et al. [26] used micro-PIV to investigate the shape of the meniscus and the flow characteristics in open rectangular microgrooves heat sinks with different inclined angle. The velocity is the highest in the middle and decreases from the middle to both side walls due to the side wall effect. It can be observed that the velocity profile is parabolic from the 3D graph and the mean velocity profile is not symmetrical due to the different roughness of two side walls. The interfacial effect such as roughness has an important influence in microscale heat transfer. An

experimental investigation of the hydrodynamic and heat transfer characteristics of water flowing through tortuous microchannels was carried out by Dai et al. [27] Their results showed that the flow recirculation and secondary flow structures (Dean vortices) induced by the bend helped to increase the heat transfer rates. Zhai et al. [28] experimentally studied hydrodynamics of deionized water flowing through the micro heat sinks with cavities and ribs with a micro-PIV system. Their experimental results explained the physical mechanism of heat transfer enhancement. The heat transfer area and flow turbulence increased, which is helpful for mixing, due to the existent of cavities and ribs.

In the existing studies in the literature, the accuracy of the micro-PIV results has been validated for fluid flow measurement. The complicated flow fields and parameters using micro-PIV are widely investigated using a micro-PIV system. The fluid flow and heat transfer phenomena in micro-pin fin heat sinks are very complicated because different shapes and dimensions of micro-pin fins may exhibit quite different fluid flow and heat transfer behaviors. Although many experimental and numerical studies of fluid flow in micro-pin fins are available, there are quite different results due to the different pin fin structures and arrangement. The fluid flow phenomena in the micro pin fins with different shapes and dimensions are very complicated and still worth to be investigated with various methods. To further explore the mechanisms of heat transfer enhancement with different micro-pin fins and to select the proper structures and arrangement of micro-pin fins, it is important to understand the fluid flow behaviors in micro-pin fins with different structures at first. In the present research, firstly, three micro pin-fins with different structures were designed and the flow fields in laminar flow in these micro-pin fins were observed and measured using a

micro-PIV system. Then, numerical simulations of the fluid flow in the same micro-pin fins were performed. The numerical simulation results of fluid flow in the three micro-pin fin heat sinks are compared to the experimental results. In order to understand the heat transfer behavior in these micro-pin fins, as the first step, numerical simulations of heat transfer in laminar flow in the three structures of micro pin fins were performed and better heat transfer performance was obtained in our study. As the fluid flow using the micro-PIV system and the experiment of heat transfer could not be performed simultaneously, the flow fields were measured with the micro-PIV and simulated with CFD while the heat transfer behaviors were only investigated with numerical simulations at this stage. The simulation results of heat transfer are helpful for the initial understanding of the phenomena and the future experiment design of heat transfer in the three micro fin pins. The corresponding better heat transfer performance of the micro pin fin heat sinks will be planned in a follow-up research.

In this paper, a micro-PIV system is employed to measure the velocity field of fluid flow in laminar flow in micro pin-fin heat sinks at first. Second, numerical simulations of the fluid flow behaviors in laminar flow were conducted and compared to the experimental results with micro-PIV. Finally, numerical simulation results of the heat transfer behaviors in the three micro heat sinks have been presented and compared. The formation and evolution of vortex behind the pin-fins are experimentally and numerically investigated to understand the physical mechanisms of heat transfer enhancement obtained from the numerical simulations of heat transfer in laminar flow in the three micro heat sinks. Reasonable analysis and explanation of the heat transfer and fluid flow mechanisms in the three micro-pin fin structures are given.

2. Description of Micro Pin-fins and Their Dimensions

The experimental sample used for optical measurement experiment in this paper is made of Polydimethylsiloxane (PDMS) which is a silicone polymer. PDMS is widely used in microfluidics due to its attractive attributes including simple and fast processing, low cost, good transparency, high chemical and electrical resistance, and good thermal stability.

First, AutoCAD was used to design the microfluidic channels on the chip layout, and the graphics is output in the format for illustrator, and photolithography mask is printed in the film by the microcomputer control printer. Then, the PDMS experimental sample is micro-fabricated in the self-built laboratory of PDMS microfluidic chip processing system. The manufacturing process is divided into 3 steps, as shown in Fig. 1, (i) the processing for SU-8 silicon mold, (ii) replica molding of PDMS and (iii) bonding and packaging processing for PDMS chip. The photograph and SEM images of the PDMS micro pin-fin fabricated in the laboratory are shown in Fig. 2.

Fig. 3 shows the schematic of two-dimensional micro-pin fins in the experimental system: (a) in-line circular micro pin-fins (C-MPF), (b) in-line square micro pin-fin (S-MPF) and (c) in-line diamond micro pin-fin (D-MPF). Table 1 lists the dimensions of the micro pin-fins. There is a rectangular region in both inlet and outlet of the channel with the dimension of $L_1 \times W = 5$ mm × 2.2 mm. The whole dimension with the micro-pin fin arrays is $L \times W \times H = 10$ mm × 2.2 mm × 0.1 mm. The pin fins are all with column hydraulic diameter $D_h = d = a_1 = a_2 = 0.2$ mm, fin height $h = 0.1$ mm, the pitch of the pin-fins in the x-axis $S_L =$

0.44 mm and the pitch in the y-axis S_T = 0.44 mm. The pin-fin row number in the x-axis direction N_x = 23 and the pin-fin row number in the y-axis direction N_y= 5.

3. Experimental Setup and Procedure

3.1. Experimental setup

Fig. 4 shows the experimental setup used in this study. It consists of three sub-systems: the experimental system (hardware system), the flow system and the image processing system (software system). The experimental system (micro-PIV, Lavision, Germany) includes a double pulse Nd: YAG laser (emitting at λ_{exc}=532 nm), a CCD camera, an inverted fluorescence microscope and a MITAS platform. The flow system includes a syringe pump, the micro flow device, fluorescent tracer particles (2 μm, E_x/E_m = 542/612 nm, Duke Scientific).The Image processing system includes a computer and Davis image processing software. The launch of the laser wavelength of 532 nm, transmitting frequency is 15 Hz, the time interval between 2 pulses is 1/15s, maximum power of 135 mJ. Inverted fluorescence microscope objective lens magnification for five times, the depth of field is 28 μm. 2 μm tracer particles density of 1.055 g/cm^3 are used to make sure the particles emitted a sufficient amount of light to be detectable.

3.2. Experimental procedure

First, the test chips are placed on the MITAS platform in order to change the location of the observed area. The middle of the plane is focused by the camera through controlling the

MITAS platform, and the fluorescent trace particles are added to the de-ionized water with a 0.03% volume concentration to give enough spatial resolution and avoid any clumps in the channel. As illustrated in the Fig. 5, when the double-pulsed laser sends a light sheet to the fluid, the particles are illuminated twice in a very short time interval. The emitted light and the images of the displacement of the particles between the time intervals of the two laser light sheets are captured as a pair of two single exposure images with the CCD camera at 1 kHz with an area of view of 2 × 2 mm^2 at full 2048 × 2048 pixels resolution under the 4 × objective.

These double frame images can be evaluated by the cross correlation. As shown in Fig. 6, a higher and unambiguous correlation peak can be obtained through double frame and double exposure. Fig. 7 shows the method of image preprocessing before calculation. The computational field is masked on the original particle image and then the image preprocessing procedure is taken to obtain a high accuracy image with bright particles and low noise which can reduce the calculation errors.

The recorded image is subdivided into several interrogation regions and the PIV evaluation is done in a multi-pulse with decreasingly smaller window size. Different interrogation window sizes are chosen to calculate the flow field as shown in Fig.8, and interrogation window sizes of 64 × 64 pixels with 50% overlap between adjacent windows shows the most moderate vector density. Finally, the velocity data are exported to the Tecplot software package (Tecplot 360) for post-processing and the streamlines and vorticity can be calculated.

4. Numerical simulation methods for fluid flow and heat transfer

In order to compare to the experimental results of fluid flow obtained in micro-PIV visualization measurements, the numerical models of micro-pin fin heat sinks were developed using the Fluent 6.3.26 to analyze the three-dimensional convective fluid flow in laminar flow at first and then the corresponding heat transfer behaviors in the three micro heat sinks.

4.1 Computational domain

The geometry of the micro-pin fins is symmetric about *x* axis, so a smaller symmetric unit is chosen as the numerical domain to simplify the computation as shown in Fig. 9. In simulation, there is a unit with a length of 5 mm upstream and downstream the channel for steady flow without heating. A constant heat flux is applied at the bottom wall (q_w = 400 Kw/m^2), while other walls are adiabatic. The length *L*, width *W'*, and height of bottom H_1 are 10, 0.88, and 0.1 mm, respectively. The structure of the micro-pin fins are the same with the experiment.

4.2 Description of mathematical model

To simplify the problem, the following assumptions were made in the simulation:

(1) Three-dimensional, incompressible, Newtonian fluid.

(2) Single-phase, steady, laminar flow.

(3) Neglect of the effects of Radiation and gravity.

(4) Constant solid and fluid properties except water viscosity changing linearly with the

temperature.

From the assumption, the fluid flow and heat transfer should be followed the convectional Navier-Stokes equations when hydrodynamic diameter greater than 100 μm and the Reynolds number below 1700 as Qu et al. [29] presented. So the broadly used steady three-dimensional governing equations for the liquid are listed respectively as follows:

The continuity equation:

$$\nabla \cdot (\rho U) = 0 \tag{1}$$

The momentum equation:

$$\rho_f \frac{\partial u}{\partial t} = -\nabla P + \mu \Delta U \tag{2}$$

The energy equation:

$$\rho_f U \cdot \nabla \cdot (c_p T) = \nabla \cdot (\lambda_f \nabla T) + \phi \tag{3}$$

where ϕ is the viscous dissipation term, which is written as

$$\phi = \mu_f \left[2\left(\frac{\partial u_x}{\partial x}\right)^2 + 2\left(\frac{\partial u_y}{\partial y}\right)^2 + 2\left(\frac{\partial u_z}{\partial z}\right)^2 + \left(\frac{\partial u_x}{\partial y} + \frac{\partial u_y}{\partial x}\right)^2 + \left(\frac{\partial u_y}{\partial z} + \frac{\partial u_z}{\partial y}\right)^2 + \left(\frac{\partial u_z}{\partial x} + \frac{\partial u_z}{\partial z}\right)^2 \right] \tag{4}$$

where $\boldsymbol{U}$ is the velocity vector, P is the pressure, T is the temperature, ρ and μ are the fluid density and dynamic viscosity respectively, and c_p is the specific heat at constant pressure.

4.3. Boundary condition and numerical methods

Apart from the governing equations, the related boundary conditions are provided as follows:

(1) All fluid-solid inter-surface of the micro-pin fins are no slip and impermeable.

(2) The initial temperature of the working fluid and the ambient air is maintained at 293 K. The heat transfer is steady state. A uniform velocity profile is applied to the fluid at the inlet.

(3) The pressure outlet is applied in the exit of the micro-pin fins, which is considered as atmosphere pressure.

(4) The constant heat flux of q_w = 400 kW/m^2 is adopted in the central area at the bottom of the heat sink.

(5) Both the two lateral planes of the numerical domain are set as “symmetry” boundary condition.

The governing equations mentioned above are all solved by FLUENT 6.3.26. A preprocessor GAMBIT is used to generate the meshes for the solver. The governing equations are discretized by using the finite control volume. The second-order upwind discretization scheme is employed to perform the computation considering the stability of solution convergence. The SIMPLEC algorithm is used to deal with the pressure-velocity coupling. The governing equations are regarded as converged once all residuals fall below10^{-7}.

4.4 Grid independency

To improve convergence speed and computing accuracy, a test of grid independence

must be examined before numerical computation. The computational domain is resolved by the irregular elements.

The pressure drops calculated respectively based on 0.468 million, 0.553 million, 0.627 million meshes were compared. The differences of pressure drops between 0.468 million, 0.553 million and 0.627 million meshes are approximately 1.4% and 0.37% respectively.

Since the differences are small, and the 0.553 million mesh system can satisfy both efficiency and accuracy as well, it is selected to conduct the calculation in this paper.

4.5 Simulation of heat transfer behaviors corresponding to the flow conditions

Numerical simulations of the heat transfer in the three heat sinks were performed corresponding to the simulations of fluid flow conditions of laminar flow in the range of Reynolds number from 40 to 300. Both average and local Nusselt numbers have been obtained to show the variations of heat transfer behaviors. The variations of average Nusselt number *Nu* versus Reynolds number *Re* have been obtained to show the overall heat transfer characteristics. The variations of local Nusselt number Nu_x versus x have been obtained to understand the mechanisms of heat transfer enhancement due to the combined function of main flow and vortexes.

The Reynolds number is defined as:

$$\mathrm{Re} = \frac{\rho_{av} u_{av} D_h}{\mu_{av}} \tag{5}$$

where ρ_{av} is the average fluid density, u_{av} is the average velocity, μ_{av} is average fluid dynamic viscosity and D_h is the hydraulic diameter: where the D_h is the diameter of for circular micro pin fin, the D_h is the side length of square pin fin and diamond pin fin, which are both 200μm

The average Nusselt number is defined as:

$$Nu = \frac{hD_h}{\lambda_{f,av}} \tag{6}$$

where A_h is the area of heater surface, A_c is interface area of fluid and solid, $T_{i,av}$ is average interface temperature, $T_{f,av}$ is the average temperature of fluid, h is the average heat transfer coefficient defined as:

$$h = \frac{qA_h}{A_c\left(T_{i,av} - T_{f,av}\right)} \tag{7}$$

The local Nusselt number is defined as:

$$Nu_x = \frac{h_l D_h}{\lambda_{f,av}} \tag{8}$$

where $T_{i,}$ $(x)$is the local interface temperature along the flow direction x, T_f $(x)$is the local temperature of fluid along the flow direction x and h_l is the local heat transfer coefficient defined as:

$$h_l = \frac{qA_h}{A_c\left[T_i(x) - T_f(x)\right]} \tag{9}$$

The velocity deviation η at the minimum cross-section of channel at the 10th row is

calculated from:

$$\eta = \frac{\overline{v_n} - \bar{v}}{\bar{v}} \tag{10}$$

where $n = 1,2\ldots5$, represents the column number of fluid channel, $\overline{v_n}$ represent the average velocity of the channel at nth column, $\bar{v}$ represents the average velocity of the five channels.

According to the definition of vorticity in two-dimensional flow, the relationship between vorticity and velocity can be obtained as

$$\Omega_z = \frac{\partial v}{\partial x} - \frac{\partial u}{\partial y} \tag{11}$$

5. Results and Discussion

In order to understand the flow characteristic with increasing of Reynolds number, the micro-PIV measurements were performed on the micro pin-fin arrays. The velocimetry was performed close to the inlet and outlet and at the center of the chip cavity in the streamwise direction at $h/2$.

5.1 Fluid flow characteristics of heat sinks

5.1.1 Velocity distribution

The velocity contours and streamlines for the Reynolds number Re = 40 in the middle of

the circular micro pin-fins obtained by experiment and simulation are shown in Fig. 10, respectively. The flow is steady. The velocity contours in experiment are in good agreement with the simulation results. Fig. 11 shows the comparison of measured velocity distribution of axis centerline at the entrance by experiment and the simulation. The maximum velocities are located in the middle of two micro-pin fins in theory, and the minimum values are downstream the micro-pin fins. The velocity distribution presents the Sine distribution consisting of periodic crests and troughs, the velocity deviation between numerical simulation and experiment is less than 3.4%.

Fig. 12 shows the velocity deviation at the minimum cross-section of channel at the 10th row, the deviation value is under ±5%, which means the velocity distribution of each channel is uniform and any channel can be chosen to represent the whole flow field.

The streamline and velocity contours of experimental are shown in Figs. 13, 14 and 15, respectively, at the center of the C-MPF, S-MPF, D-MPF for the Reynolds number ranging from 10 to 200. The results indicate that at low Reynolds numbers, the flow of C-MPF is steady and there is no vortex shedding downstream the pins. With increasing the Reynolds number, the stagnant recirculation zones and vortex formation are observed behind the pins.

Fig. 13(a), 14(a) and 15(a) show that the flow of C-MPF, S-MPF, D-MPF are all steady for Re=10 and there are no vortex shedding downstream the pins, the velocity of S-MPF in the centerline is highest. For Re = 40, there is still no vortex behind the pin-fins of C-MPF, but there gradually appear small symmetric vortices of S-MPF, and the vortexes are more complicated of D-MPF. With the increase of Reynolds numbers, the flow becomes more unstable, and different vortex structures are observed behind the pins. Figs. 13 (c) and (d)

show some sample flow patterns observed such as symmetric vortices and a single and a collapsed vortex between pins. It can be obviously observed from Figs. 15 (c) and (d) that big complete symmetric vortices are behind the pin-fins of D-MPF, which can effectively improve the mixing of fluid.

5.1.2 Vorticity distribution

Fig. 16 shows the distribution of vortex around pin-fin under different Reynolds number *Re*. For lower Reynolds numbers, the vortex area is small and the distribution is mainly around the cylinder in the vertical direction of flow. The diffusion of vortex in *x*-axis is better than because of the small kinetic energy of the mainstream. When the Reynolds number increases, the vorticity field of the pin-fins in front covers the back pin-fins, the effect of the latter to the vorticity field increases.

When the viscous fluid flows around the fins, there is a laminar boundary layer near the wall as shown in Fig. 17. The point M is the middle point on the wall of micro pin-fin along the flow direction. The point S is boundary layer separation point which is defined as the boundary between the forward flow and backward flow of the fluid near the wall viscous fluid flow around.

Fig. 18 shows the velocity boundary layer in the pin-fin of C-MPF at *Re* = 100. The velocity and pressure is highest and lowest, respectively at the outer edge of the point M's boundary layer. the streamlines of the outer flow converge, resulting in an increase of the free stream velocity Upstream of the point M is accelerating region, $U(x)$ and a consequent fall of

pressure with *x*, as $\frac{\partial u}{\partial x} > 0$, $\frac{dp}{dx} < 0$. Downstream of the point M is decelerating region, the streamlines diverge, resulting in a decrease of *U(x)* and a rise in pressure, as $\frac{\partial u}{\partial x} > 0$, $\frac{dp}{dx} < 0$. At the wall, the boundary layer equation becomes $\mu\left(\frac{\partial^2 u}{\partial y^2}\right)_{wall} = \frac{dp}{dx}$. At point M, $\frac{dp}{dx} = 0$, $\frac{\partial^2 u}{\partial y^2}$=0, the curvature of the velocity profile at the wall is zero, so it is an inflection of point. The velocity distribution of the whole boundary layer is a smooth curve, and there is no boundary layer separation.

With the flow of fluid, there is a point S, the $\frac{\partial u}{\partial y} = 0$ on the wall. The kinetic energy is consumed by viscous force and adverse pressure gradient force. The flow of boundary layer is separated to two parts, adverse pressure gradient brings the lower fluid into back flow, the main flow brings the upper fluid continue to flow, and the vortex is generated.

5.1.3 Pressure drop analysis

Fig. 19 shows the variation of pressure drop versus the Reynolds number from the numerical simulation. It can be seen that with increasing the Reynolds number, the pressure drop develops as a parabolic form. When the Reynolds number is small, the velocity is low, the fluid viscosity and the roughness of the pin-fins causes the boundary layer to form between pin fins very easily. The end wall effect is significant and the wall shear stress is large, which are the main factors to cause pressure drop. Therefore, the pressure drops in C-MPF, S-MPF and D-MPF are nearly the same. As the flow rate increases constantly, the fluid velocity near the wall is large and the end wall effect weakens gradually. The viscous and blocking effects on the fluid exerted by the upper, lower and side walls of the pin fins,

rise rapidly, which caused the boundary layer to separate from the wall of pins, and vortex forming in the wake starts to shed. As shown in Figs. 13, 14 and 15, the vortex forming and shedding in D-MPF is earlier than those in the other two micro-fins, therefore the pressure drops are the highest among the three micro pin fins.

5.2 Heat transfer characteristics of heat sinks

Fig. 20 shows the average Nusselt number of C-MPF, S-MPF, D-MPF improve with the increase of *Re*. When *Re* is small the flow velocity is low, there is a flow stagnation zone behind the S-MPF and D-MPF. However, there are still a close velocity of the main flow and the back flow behind the pin-fins of C-MPF, which lead to a higher *Nu* with a small *Re*. Because of the low velocity, the impact of flow against the front two side walls of the diamond pin-fins is very small, and the *Nu* of C-MPF is highest. With the increase of *Re*, the vortex behind the pin-fins grow gradually, compared with the square pin-fins, the vortex can be easiest involved in the main flow of the circular and diamond pin-fins because of the high deceleration and pressurization zone. Therefore, the comprehensive of the impact of the main flow to the front side wall and the high vortex intensity behind the diamond pin-fins lead to the best heat transfer enhancement.

Fig. 21 shows the local *Nu* along the flow direction at the center of channel. At the entrance section, the temperature of the flow is low, so the local Nu_x shows the best heat transfer coefficient. The effect of heat transfer enhancement decreases gradually along the flow direction. At the exit section, there is a small increase of the heat transfer strengthening because of the three-dimensional heat conduction. For low Reynolds numbers, C-MPF

presents the best heat transfer enhancement effect. With the increase of *Re*, the heat transfer intensification are all improved and the D-MPF has the most obvious heat transfer enhancement effect.

It should be mentioned that the heat transfer behaviors are obtained only from the numerical simulations. Both the experimental and simulated results of fluid flow may explain the heat transfer behaviors reasonably. It is thus suggested that further experiments on heat transfer be conducted in future.

5.3 Fluid flow and heat transfer mechanisms analysis

It is interesting to analyze and explain the fluid flow and heat transfer observed phenomena in this study according to their physical mechanisms here. For the S-MPF, the back of the square pin-fins do not facilitate the fluid flow and there is a stagnation zone in the back of the micro pin-fins. In the meantime, due to the inertia force focusing on the middle-channel where there is no pin fin, the fluid is easy to flow faster in the middle channel than others. Among the three structures, the D-MPF has the smallest cross-section area and the flow velocity should have been the highest. However, according to the experimental results, the flow velocity is not the highest. This may be attributed to the shape of the D-MPF structure and the arrangement. The fluid is much easier to flow to the back of the D-MPF due to the enlargement of the flow channel in the back, the fluid flow is more uniformly distributed in the D-MPF and therefore the flow velocity is decreased and not the highest.

For the D-MPF, the flow disturbance increases in both the front and back of the D-MPF with increasing Re. The boundary layer separates from the wall and the vortex forms and

sheds in both the front and back, which significantly increase the pressure drop in the D-MPE. Therefore, the experimental results of the highest pressure drop reflect the flow phenomena. For the C-MPF, due to it is circular structure, the fluid is much easier to flow to the back compared to the other two structures. The flow disturbance becomes weaker than those in the other two structures. Therefore, the pressure drop in C-MPF is the smallest. For the S-MPF, the fluid flows fast in the middle channel because of the inertia force which leads to a higher velocity in the middle channel. The flow disturbance in the front row of micro pin-fins becomes strong but the influence in the back row becomes weak. Overall, the pressure drop in the S-MPF is slightly larger than in the C-MPF.

For the C-MPF, all the walls of micro pin-fins are effective in heat transfer and the back flow easily returns into the mainstream facilitate the heat transfer at the back of the micro pin-fins. However, for the S-MPF, due to flow stagnation zone in the back of the micro pin-fins and the flow velocity is low, the heat transfer becomes weak. Furthermore, the fluid flows fast in the middle channel because of the inertia force. Therefore, the effective heat transfer area only includes the front wall of front row and two sides wall normal to the flow direction in the S-MPF. The effective heat transfer area is thus smaller than the C-MPF and the overall heat transfer in S-MPF is worse than that in the C-MPF. Therefore, the Nusselt numbers of circular pin fins is higher those in the square pin fins.

6. Conclusions

Micro-PIV flow visualization technology and numerical simulations with CFD were

used to study the laminar flow and heat transfer characteristics in the three micro pin-fin bundles heat sinks. The experimental results are compared to the numerical simulation results. Good agreements have been obtained. The following conclusions have been obtained:

1) A two-dimensional flow field velocity distribution in the middle plane of the channel was measured for a Reynolds number *Re* = 40. The velocity distribution in each channel is uniform in the experiment. The experimental results agree with the results of numerical simulation using CFD.
2) The normalized time averaged streamline patterns and instantaneous velocity contours at the center of the C-MPF, S-MPF and D-MPF for the Reynolds number Re = 10 to 200 have been obtained. At low Reynolds numbers, the flow is steady and there is no vortex shedding downstream the pins. With increasing the Reynolds number, the stagnant recirculation zones gradually become unstable and vortexes having various sizes, structures and at different positions have been observed behind the micro pin fins. Of the three types of micro pin fin heat sinks, the vortexes in the D-MPF occur the earliest and present the most complicated structure, which can effectively improve the mixing of fluid.
3) At low Reynolds number *Re* = 40, the area of vorticity field is small. With increasing the Reynolds number, the influence on vorticity field of the front fin caused by the back fin becomes stronger. With increasing the Reynolds number, the kinetic energy of the boundary layer is consumed by the viscous force and adverse pressure gradient force, the flow in the boundary layer is separated to two parts. The adverse pressure gradient brings the lower fluid into back flow, the main flow brings the upper fluid continue to flow, and

the vortex is generated.

4) With increasing the Reynolds number, the pressure drop evolves as a parabolic form. At low Reynolds numbers, the end wall effect is significant and the wall shear stress is large, which are the main factors to cause pressure drops. With increasing the Reynolds number, the boundary layer separates from the wall of the pin fins, and the vortexes forming in the wake start to shed, which lead to the higher pressure drop. The vortex forming and shedding in the D-MPF is earlier than the other two structures and thus lead to the highest pressure drops among the three types of micro pin fin heat sinks.
5) With increasing the Reynolds number, the vortexes behind the micro pin-fins grow gradually. Compared to the S-MPF and C-MPF, the vortexes can be much easily involved in the main flow in the DMPF because of the high deceleration and pressurization zone. Therefore, the combined impact of the main flow to the front side wall and the high vortex intensity behind the D-MPF lead to the best heat transfer enhancement among the three micro pin fin heat sinks.
6) Both the experimental and simulated results of fluid flow may explain the simulated heat transfer behaviors reasonably. Further experiments on heat transfer should be conducted in future.

Acknowledgements

This work was supported by the National Natural Science Foundation of China (No. 51576005) and the Beijing Natural Science Foundation (3142004).

Nomenclature

a_1 side length of square pin fin, m

a_2 side length of diamond pin fin, m

c_p specific heat at constant pressure, J/kg·K

D_h hydraulic diameter, m

d diameter of circular pin fin, m

H pin fin height, m

H_1 pin fin height, m

h height of pin-fin in the simulation, m, heat transfer coefficient, W/m^2K

L length of the micro-pin fin arrays and test channels, m

L_1 channel length before and after the micro-pin fin arrays, m

N_x number of pin fin along x-axis

N_y number of pin fin cross x-axis

Nu Nusselt number, $[hD_h/k_f]$

P pressure, Pa

q_w wall heat flux, W/m^2

Re Reynolds number $[vD_h/\mu]$

S_L pitch of micro pin fins along the channel length (x-axis), m

S_T pitch of the micro pin fins along the channel width (y-axis), m

T temperature, K

u_i the velocity component, m/s

u_j the velocity component, m/s

$\bar{v}$ the average velocity of the five channels, m/s

$\bar{v}_n$ the average velocity of the channel at nth column, m/s

W width of the micro-fin arrays and test channels, m

W' width of the micro-fin arrays channels in simulation, m

w vortex, 1/s

Greeks

η velocity deviation, Eq. (5)

λ thermal conductivity, W/m·K

μ dynamic viscosity, Ns/m^2

ρ fluid density, kg/m^3

Ω_z vorticity, Eq. (9)

Subscripts

f fluid

i indices in the Einstein summation convention

j indices in the Einstein summation convention

l local

n the column number of fluid channel

x x axis

y y axis

av average

References

[1] D.B. Tuckerman, R.F.W. Pease, High performance heat sinking for VLSI, EEE Electron Device Letter 15 (1981) 126-129.

[2] J.R. Thome, The new frontier in heat transfer: microscale and nanoscale technologies, Heat Transfer Eng. 27(9) (2006) 1-3.

[3] L. Cheng, Microscale and nanoscale thermal and fluid transport phenomena: Rapidly developing research fields, Int. J. Microscale Nanoscale Thermal Fluid Transport Phenomena 1 (2010) 3-6.

[4] L. Cheng and G. Xia, Fundamental issues, mechanisms and models of flow boiling heat transfer in microscale channels, Int. J. Heat Mass Transfer, Vol. 108 (Part A) (2017) 97-127.

[5] J.R. Thome, State-of-the art overview of boiling and two-phase flows in microchannels, Heat Transfer Eng. 27(9) (2006) 4-19.

[6] L. Cheng and J. R. Thome, Cooling of Microprocessors Using Flow Boiling of CO_2 in a Micro-Evaporator: Preliminary Analysis and Performance Comparison, Appl. Therm. Eng. 29 (2009) 2426-2432.

[7] D.B. Tuckerman, R.F.W. Pease, Ultrahigh thermal conductance microstructures for cooling integrated circuits, in: Proceedings of 32nd Electronics Components Conference,

San Diego, CA, 1981,pp. 145-149.

[8] Y. Peles, A. Kosar, C. Mishra, B. Schneider, Forced convective heat transfer across a fin micro heat exchanger, Int. J. Heat Mass Transfer 48 (2005) 3615-3627.

[9] A. Kosar, C. Mishra, Y. Peles, Laminar flow across a bank of low aspect ratio micro pin fins, J. Fluids Eng. 127(3) (2005) 419-430.

[10] A. Kosar, Y. Peles, Thermal-hydraulic performance of MEMS-based pin fin heat sink, J. Heat Transfer 128 (2006)121-131.

[11] A. Kosar, Y. Peles, Micro scale pin fin heat sink-Parametric performance evaluation study, IEEE Tran. Comp. Pack. Tech. 30 (4) (2007) 855-865.

[12] R.S. Prasher, J. Dirner, J.Y. Chang, A. Myers, D. Chau, D. He, S. Prstic.Nusselt number and friction factor of staggered arrays of low aspect ratio micro pin-fins under cross flow for water as fluid, J. Heat Transfer 192 (2007) 141-153.

[13] T.M. Jeng, S.C. Tzeng, Pressure drop and heat transfer of square pin-fin arrays in in-line and staggered arrangements, Int. J. Heat Mass Transfer 50(2007) 2364-2375.

[14] Z.Y. Shi, T. Dong, Entropy generation and optimization of laminar convective heat transfer and fluid flow in a microchannel with staggered arrays of pin fin structure with tip clearance, Energ. Convers. Manage. (94) 2015 493–504.

[15] G.D. Xia, D.D. Ma, Y.L. Zhai, Y.F. Li, R. Liu, M. Du, Experimental and numerical study of fluid flow and heat transfer characteristics in microchannel heat sink with complex structure, Energ. Convers. Manage. (105) 2015 848–857.

[16] C.P. Zhang, Y.F. Lian, C.H. Hsu, J.T. Teng, S. Liu, Y.T. Chang, R. Greif, Investigations of thermal and flow behavior of bifurcations and bends in fractal-like microchannel

networks: Secondary flow and recirculation flow, Int. J. Heat Mass Transfer 85 (2015) 723–731.

[17] J. Zhao, S.B. Huang, L. Gong, Z. Q. Huang, Numerical study and optimizing on micro square pin-fin heat sink for electronic cooling, Appl. Therm. Eng. 93 (2016) 1347–1359.

[18] T. Izci, M. Koz, A. Kosar, The Effect of Micro Pin-Fin Shape on Thermal and Hydraulic Performance of Micro Pin-Fin Heat Sinks, Heat Transfer Eng. 36(17) (2015) 1447–1457.

[19] A. Renfer, M. K. Tiwari, R. Tiwari, F. Alfieri, T. Brunschwiler, B. Michel, D. Poulikakos, Microvortex-enhanced heat transfer in 3D-integrated liquid cooling of electronic chip stacks, Int. J. Heat Mass Transfer 65 (2013) 33–43.

[20] D. Sinton, Microscale flow visualization, Microfluid Nanofluid 1 (2004) 2-21.

[21] J.G. Santiago, S.T. Wereley, C.D. Meinhart, A particle image velocimetry system for microfluidics, Exp. Fluids 25(4)(1998) 316-319.

[22] C.D. Meinhart, S.T. Wereley, J.G. Santiago, PIV measurements of a microchannel flow, Exp. Fluids 27(5) 1999414-419.

[23] G. Silva, N. Leal, V. Semiao, Determination of microchannels geometric parameters using micro-PIV, Chem. Eng. Res. Des. 87 (2009) 298-306.

[24] J. Jung, C.J. Kuo, Y. Peles, M. Amitay, The flow field around a micropillar confined in a microchannel, Int. J. Heat and Fluid Flow 26(2012) 118-132.

[25] A. Renfer, M.K. Tiwari, T. Brunschwiler, B. Michel, D. Poulikakos, Experimental investigation into vortex structure and pressure drop across microcavities in 3D integrated electronics, Exp. Fluids 51(2011) 731–741.

[26] D. Yu, X.G. Hu, C.H. Guo, T. Wang, X. Xu, D. Tang, X. Nie, L. Hu, F. Gao, T.

Zhao,Investigation on meniscus shape and flow characteristics in open rectangular microgrooves heat sinks with micro-PIV, Appl. Therm. Eng. 61(2013) 723–731.

[27] Z.H. Dai, D.F. Fletcher, B.S., Haynes, Impact of tortuous geometry on laminar flow heat transfer in microchannels, Int. J. Heat Mass Transfer 83(2015) 382- 398.

[28] Y. L. Zhai, G. D. Xia, Z. Chen, Z.H. Li, Micro-PIV study of flow and the formation of vortex in micro heat sinks with cavities and ribs, Int. J. Heat Mass Transfer 98 (2016) 380–389.

[29] W. Qu, I. Mudawar, Experimental and numerical study of pressure drop and heat transfer in a single-phase micro-channel heat sink, Int. J. Heat Mass Transfer 43 (2002) 2549-2565.

List of Table Caption

List of Figure Captions

Fig.1 Manufacturing process of PDMS experimental sample.

Fig.2 Photograph and SEM images of the PDMS micro pin-fin (a) In-line circular micro pin-fin (C-MPF); (b)In-line square micro pin-fin (S-MPF); (c) In-line diamond micro pin-fin (D-MPF).

Fig. 3 Schematic of two-dimensional micro-pin fins (a) In-line circular micro pin-fin (C-MPF); (b) In-line square micro pin-fin (S-MPF); (c) In-line diamond micro pin-fin (D-MPF).

Fig. 4 The experimental setup with Micro-PIV.

Fig. 5 Principle of micro-PIV system.

Fig. 6 Evaluation of micro-PIV recordings using cross-correlation.

Fig. 7 Method of image preprocessing (a) focused plane in the middle of the micro pin-fin; (b) original particle image; (c) mask definition of the computational field; (d) image after preprocessing.

Fig. 8 Computation results of different interrogation window sizes (a) interrogation window size of 128 × 128 pixels with 50% overlap; (b) interrogation window size of 64 × 64 pixels with 50% overlap; (c) interrogation window size of 32 × 32 pixels with 50% overlap.

Fig. 9 Schematic diagram of three-dimensional numerical domain of C-MPF.

Fig. 10 Comparison of velocity contours and streamlines for *Re* = 40 (a) experimental data; (b) simulation results.

Fig. 11 Distribution of axis centerline velocity at the entrance for *Re* = 40.

Fig. 12 Experimental velocity deviation at the minimum cross-section for *Re* = 40.

Fig. 13 Velocity contours and streamlines of C-MPF at different *Re* (a) *Re* = 10; (b) *Re* = 40; (c) *Re* = 100; (d) *Re* = 200.

Fig. 14 Velocity contours and streamlines of S-MPF at different *Re* (a) *Re* = 10; (b) *Re* = 40; (c) *Re* = 100; (d) *Re* = 200.

Fig. 15 Velocity contours and streamlines of D-MPF at different *Re* (a) *Re* = 10; (b) *Re* = 40; (c) *Re* = 100; (d) *Re* = 200.

Fig. 16 Distribution of vortex around C-MPF at different *Re* (a) *Re* = 40; (b) *Re* = 100.

Fig. 17 Boundary layer near the wall when the viscous fluid flows around the fins

Fig. 18 Velocity distribution of boundary layer behind pin-fin of C-MPF at Re = 100.

Fig. 19 Variation of pressure drop versus Re.

Fig. 20 Numerical results of Nu versus Re.

Fig. 21 Numerical results of local Nusselt number Nu_x versus x for different Re (a) C-MPF; (b) S-MPF; (c) D-MPF.

Table 1 Dimensions of the micro pin fin heat sink (Unit: mm).

a_1	a_2	D_h	d	H	h	L	L_1	S_L	S_T	W
0.2	0.2	0.2	0.2	0.1	0.1	10	5	0.44	0.44	2.2

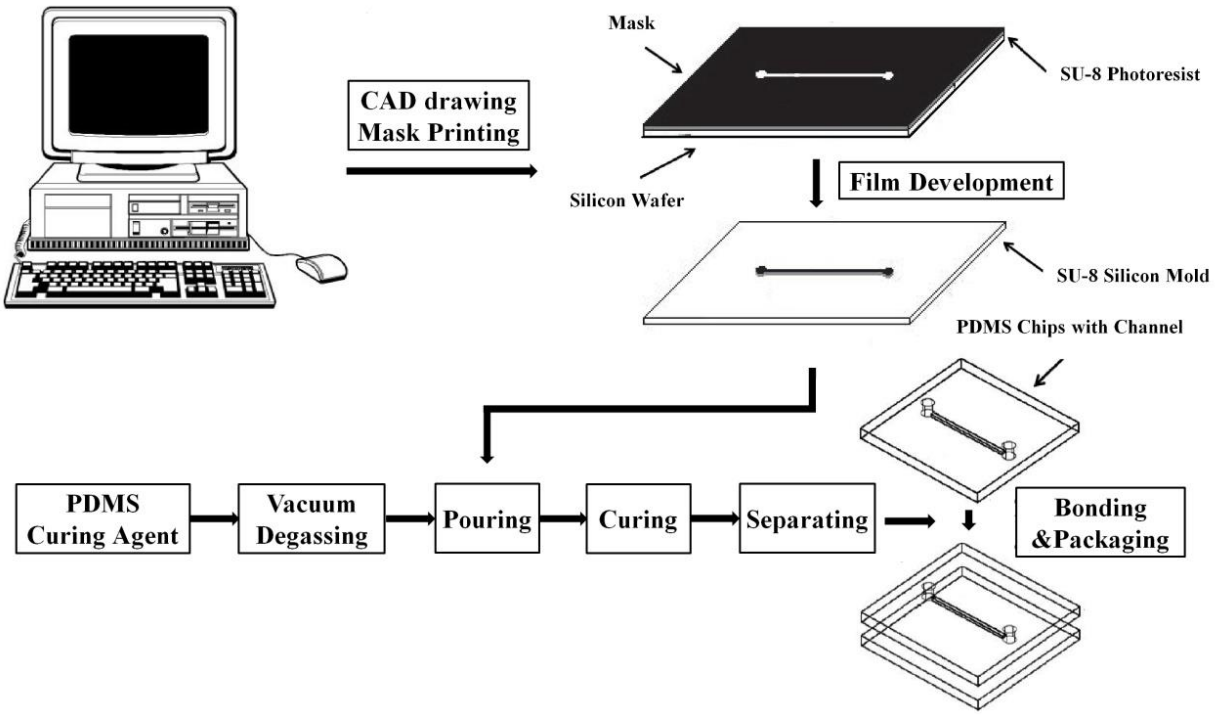

Fig. 1 Manufacturing process of PDMS experimental sample.

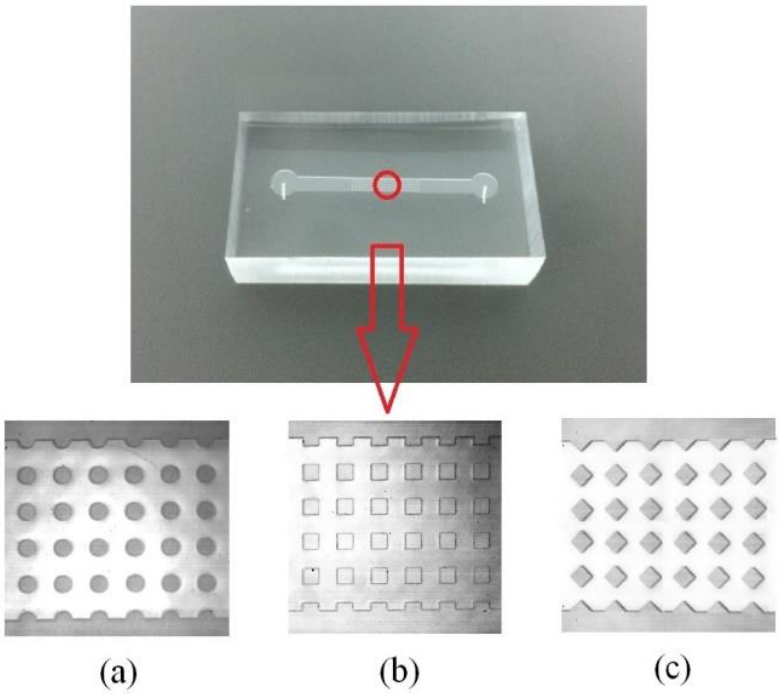

Fig. 2 Photograph and SEM images of the PDMS micro pin-fin (a) In-line circular micro pin-fin (C-MPF), (b) In-line square micro pin-fin (S-MPF), (c) In-line diamond micro pin-fin (D-MPF).

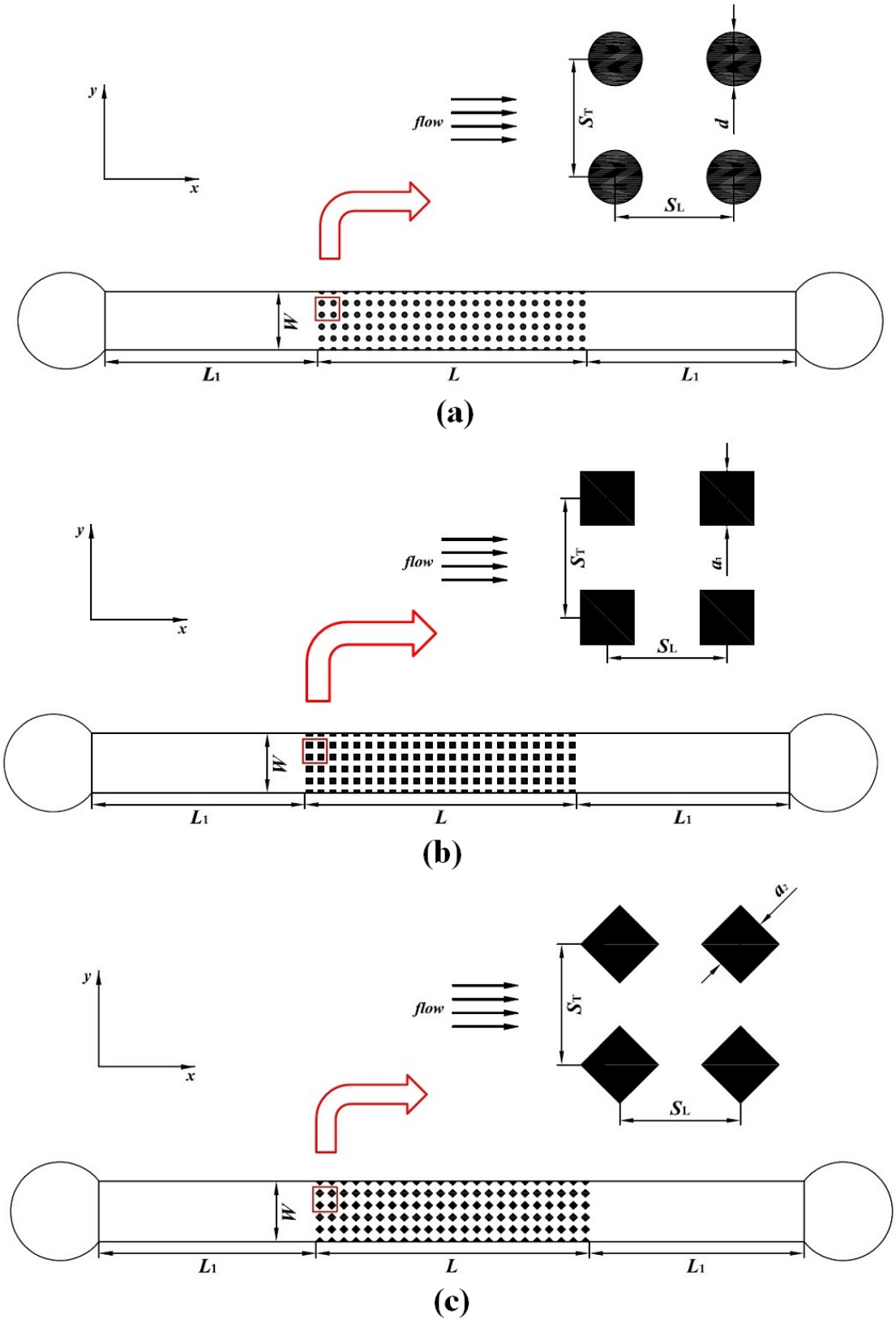

Fig. 3 Schematic of two-dimensional micro-pin fins (a) In-line circular micro pin-fin (C-MPF), (b) In-line square micro pin-fin (S-MPF), (c) In-line diamond micro pin-fin (D-MPF).

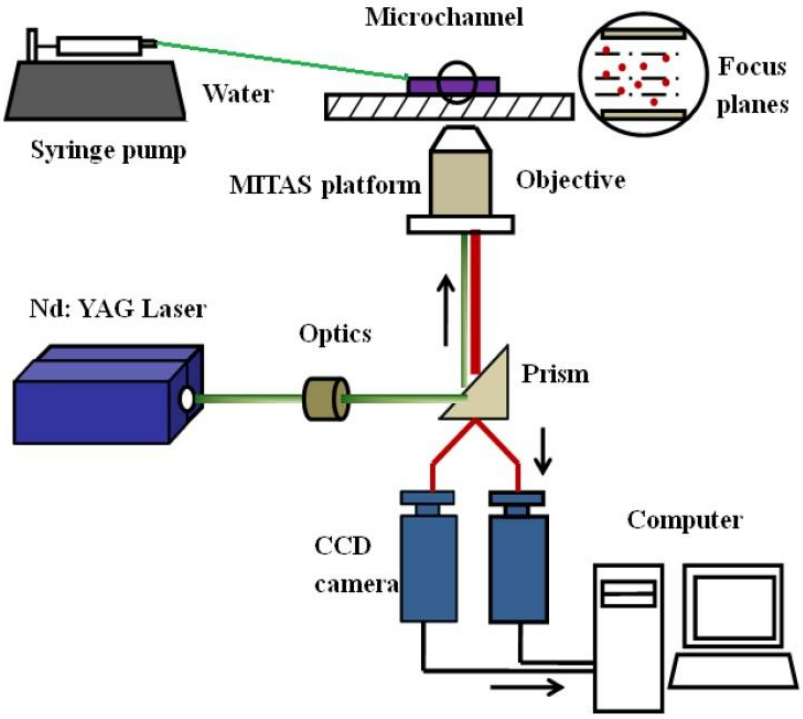

Fig. 4 The experimental setup with Micro-PIV.

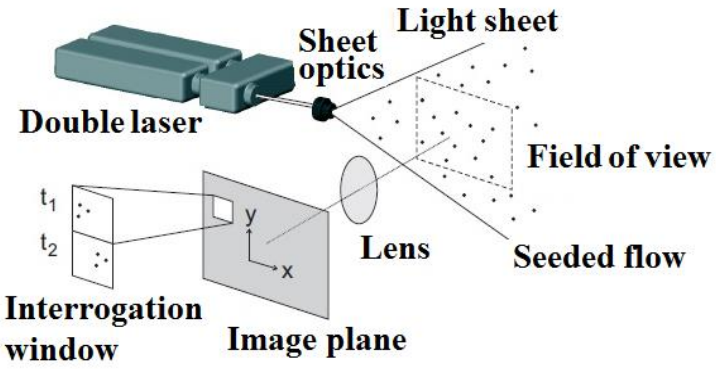

Fig. 5 Principle of micro-PIV system.

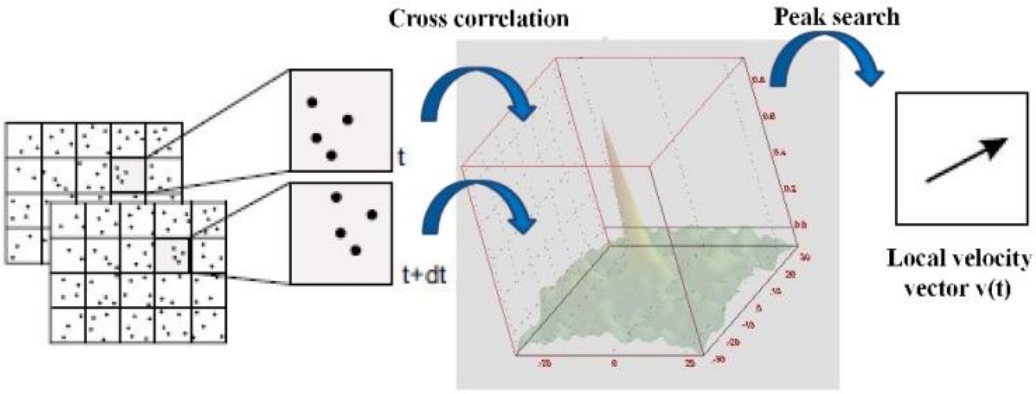

Fig. 6 Evaluation of micro-PIV recordings using cross-correlation.

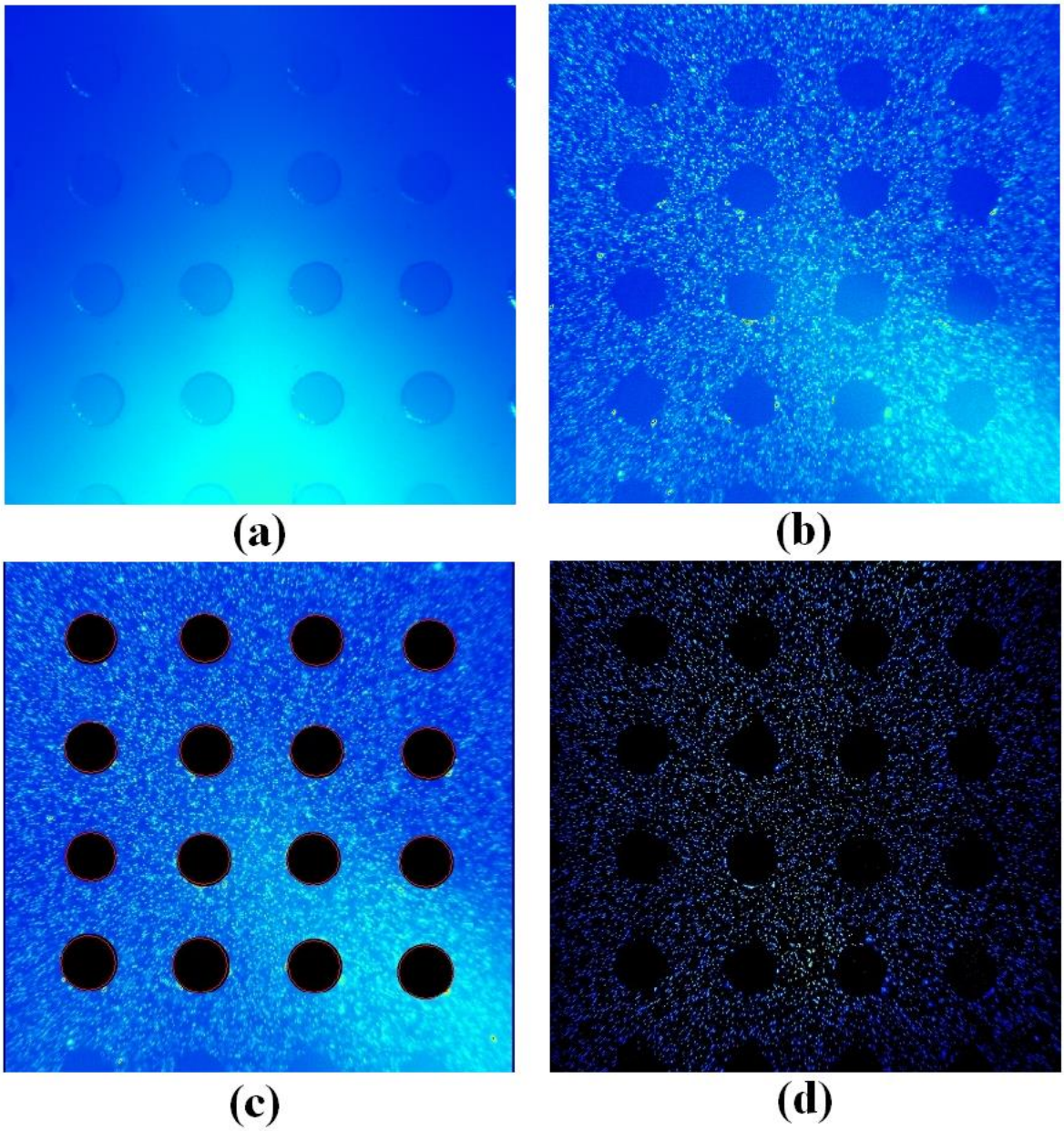

Fig. 7 Method of image preprocessing (a) focused plane in the middle of the micro pin-fin, (b) original particle image, (c) mask definition of the computational field, (d) image after preprocessing.

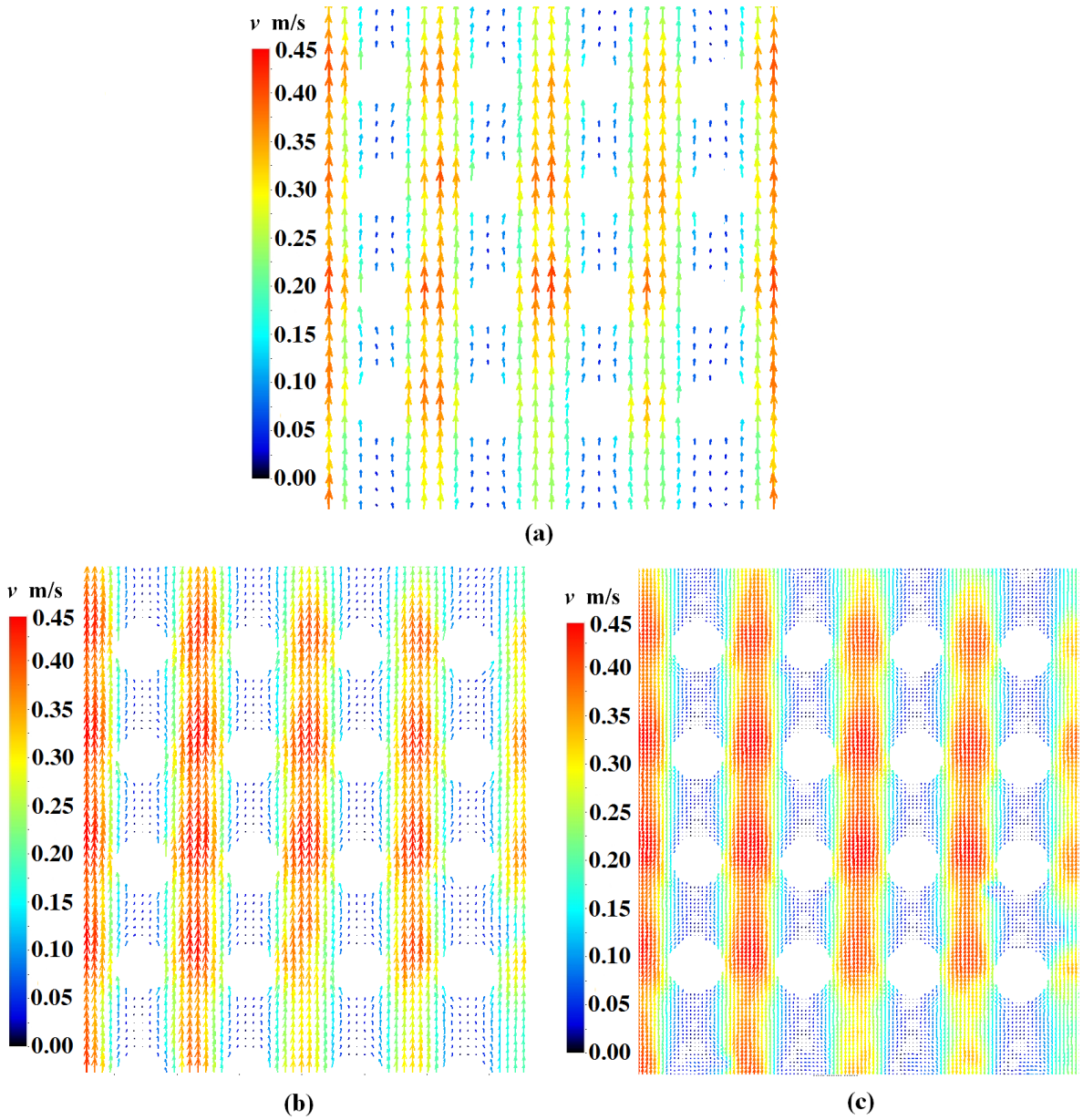

Fig. 8 Computation results of different interrogation window sizes (a) interrogation window size of 128 × 128 pixels with 50% overlap (b) interrogation window size of 64 × 64 pixels with 50% overlap (c) interrogation window size of 32 × 32 pixels with 50% overlap.

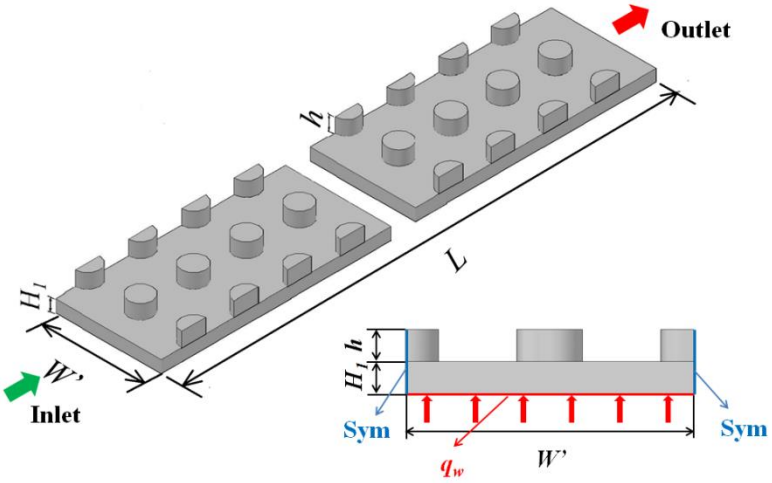

Fig. 9 Schematic diagram of three-dimensional numerical domain of C-MPF.

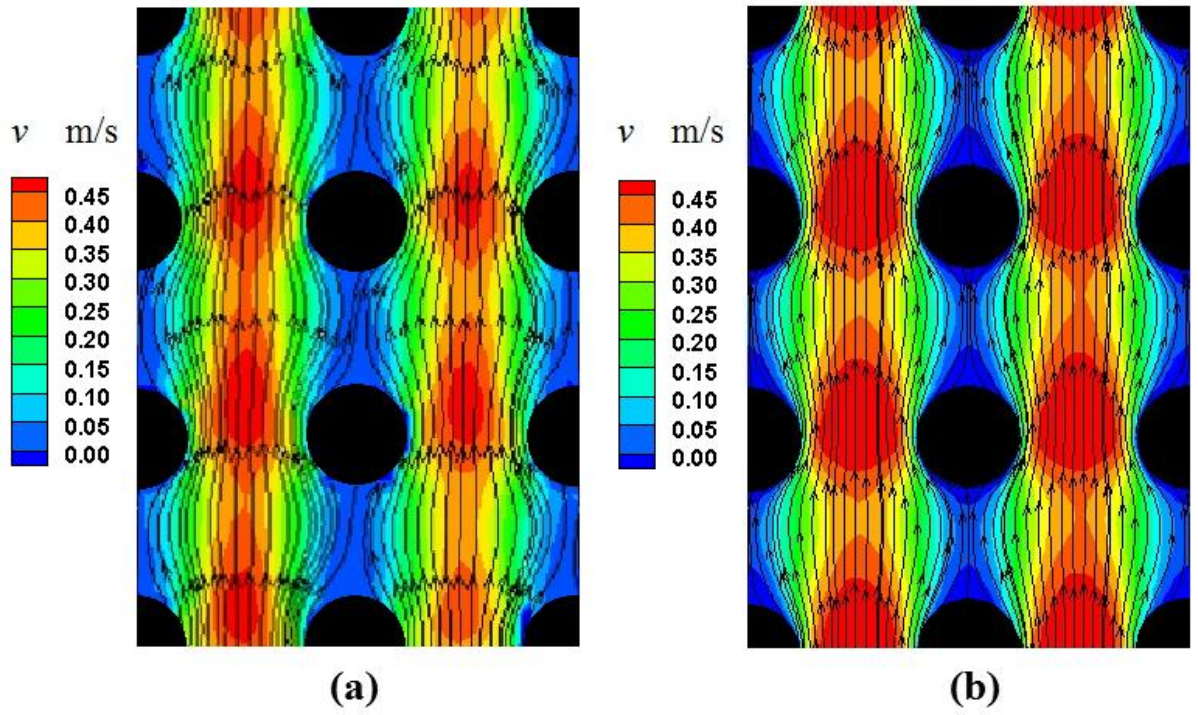

Fig. 10 Comparison of velocity contours and streamlines for *Re* = 40 (a) experimental data; (b) simulation results.

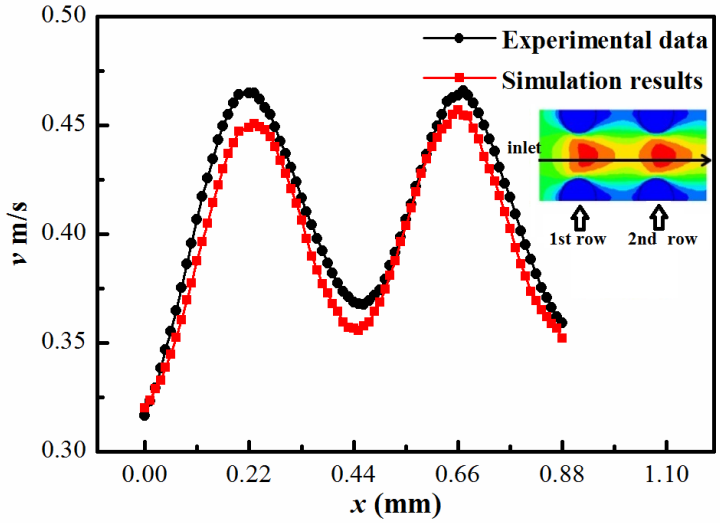

Fig. 11 Distribution of axis centerline velocity at the entrance in front of the first row of micro pin-fins for *Re* = 40.

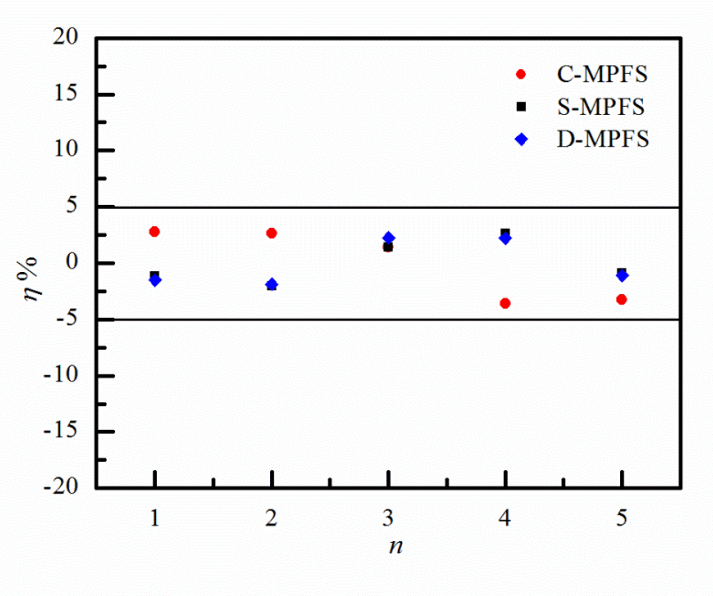

Fig. 12 Experimental velocity deviation at the minimum cross-section for *Re* = 40.

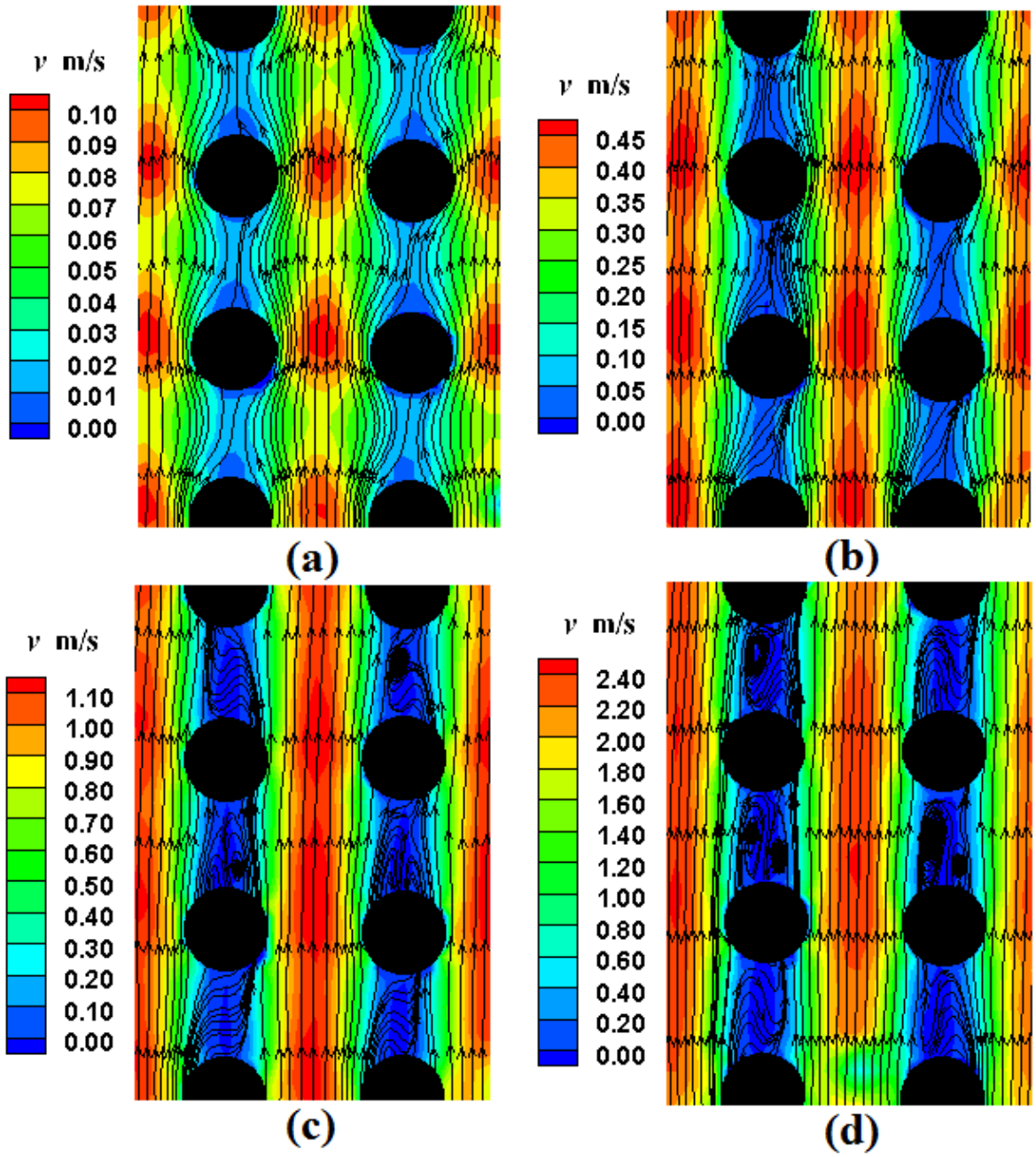

Fig. 13 Velocity contours and streamlines of C-MPF at different *Re* (a) *Re* = 10; (b) *Re* = 40; (c) *Re* = 100; (d) *Re* = 200.

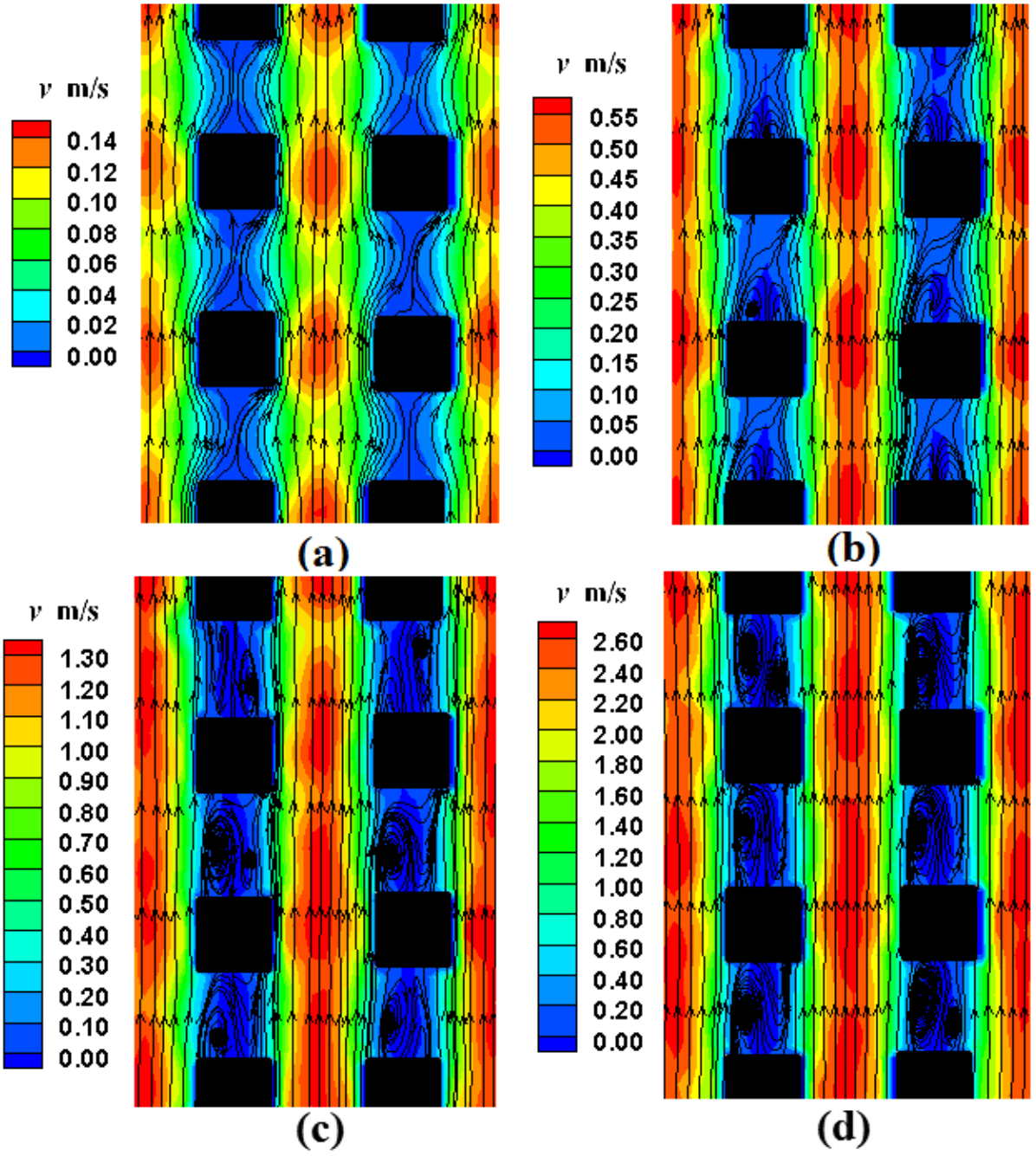

Fig. 14 Velocity contours and streamlines of S-MPF at different *Re* (a) Re = 10; (b) *Re* = 40; (c) *Re* = 100; (d) *Re* = 200.

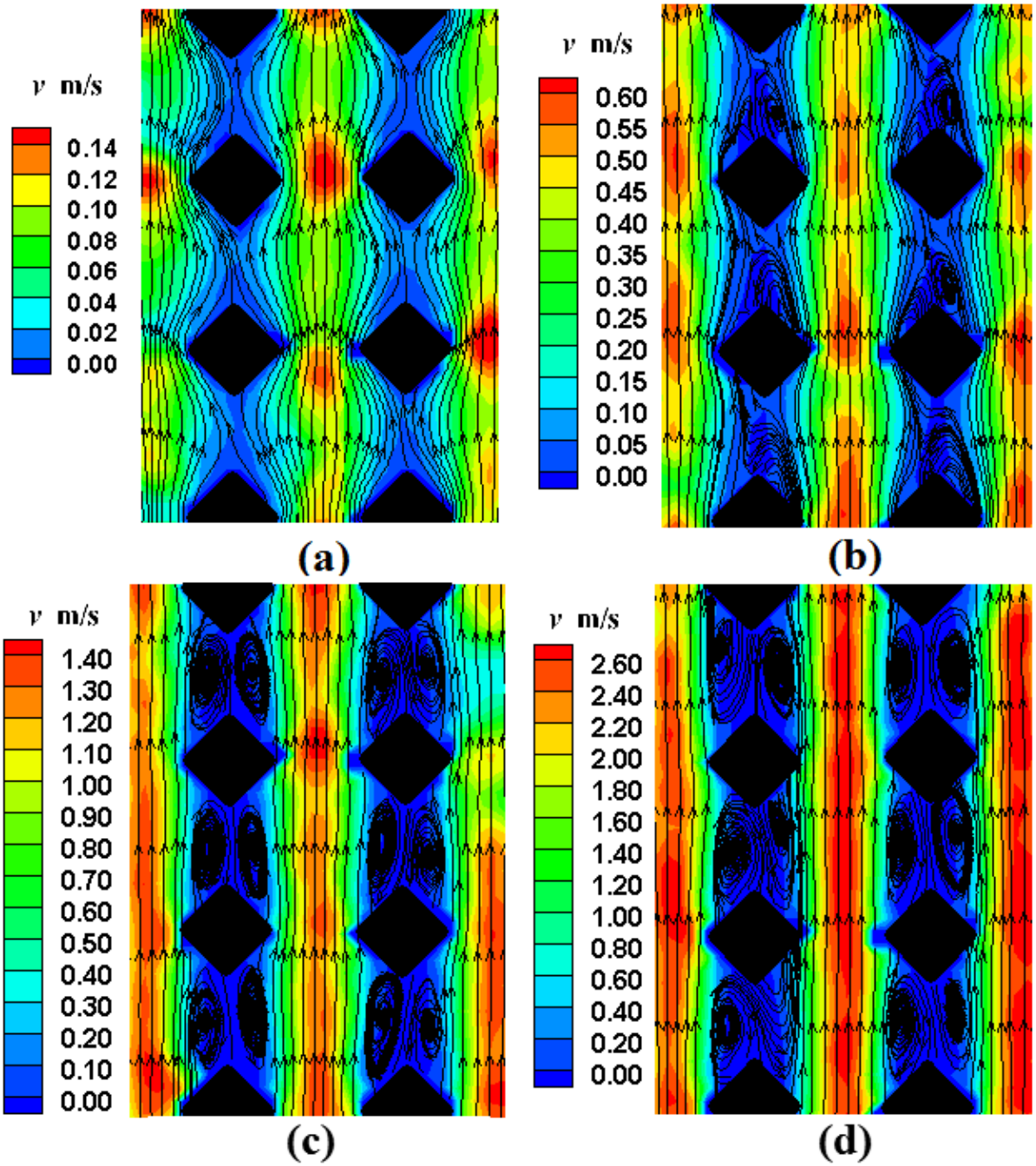

Fig. 15 Velocity contours and streamlines of D-MPF at different *Re* (a) *Re* = 10; (b) *Re* = 40; (c) *Re* = 100; (d) *Re* = 200.

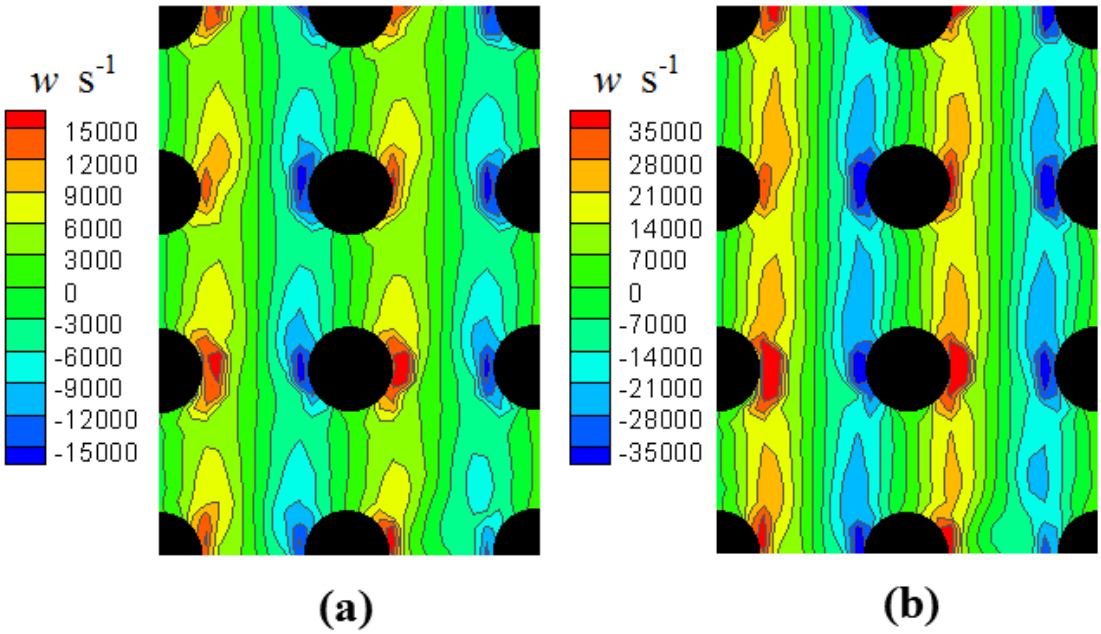

Fig. 16 Distribution of vortex around C-MPF at different *Re* (a) *Re* = 40; (b) *Re* = 100.

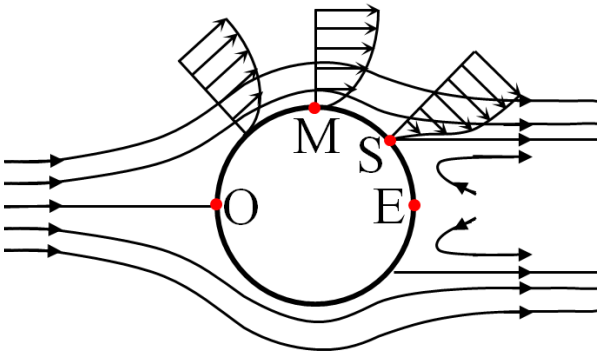

Fig. 17 Boundary layer near the wall when the viscous fluid flows around the fins.

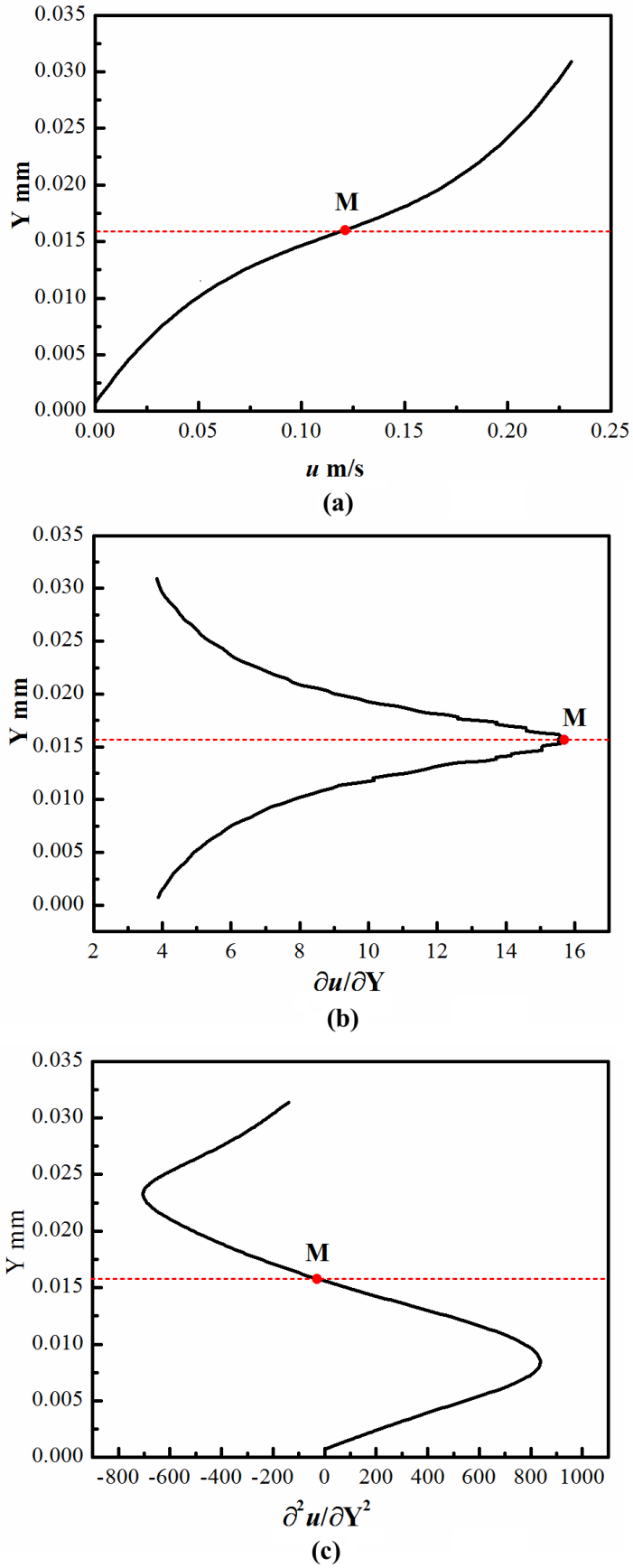

Fig. 18 Velocity distribution of boundary layer behind pin-fin of C-MPF at *Re* = 100.

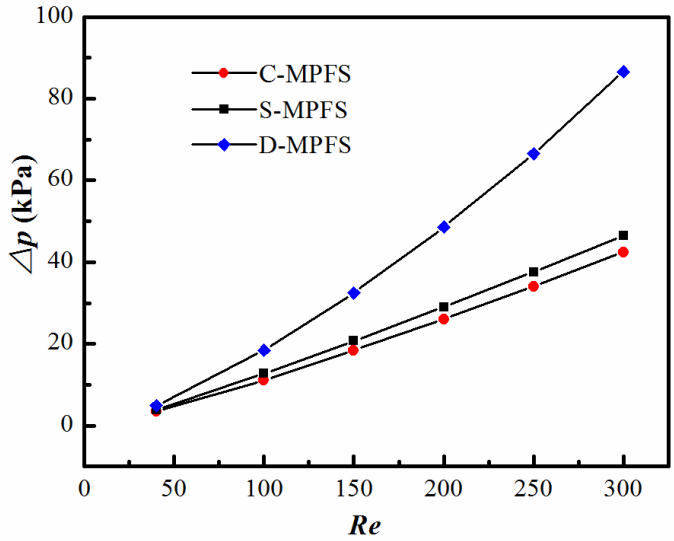

Fig. 19 Variation of pressure drop versus *Re*.

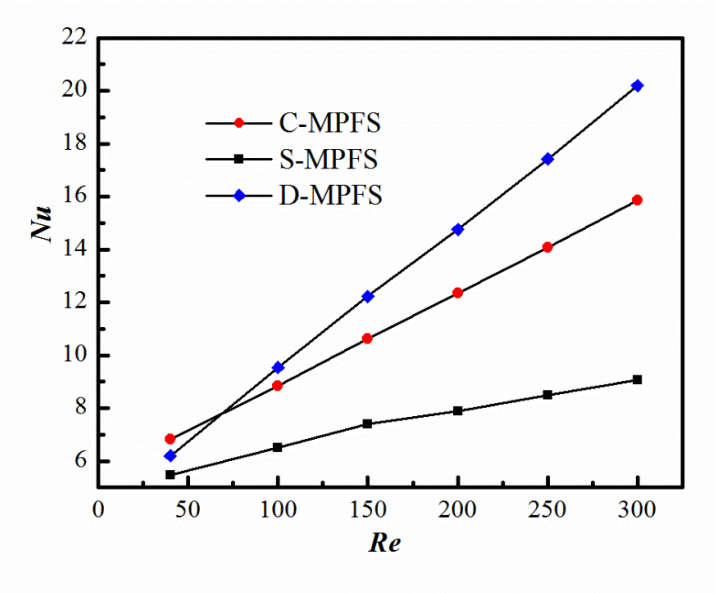

Fig. 20 Numerical results of *Nu* versus *Re*.

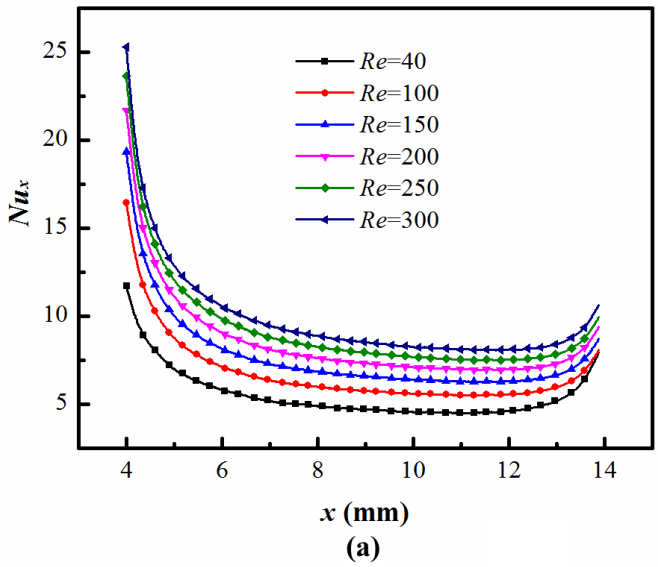

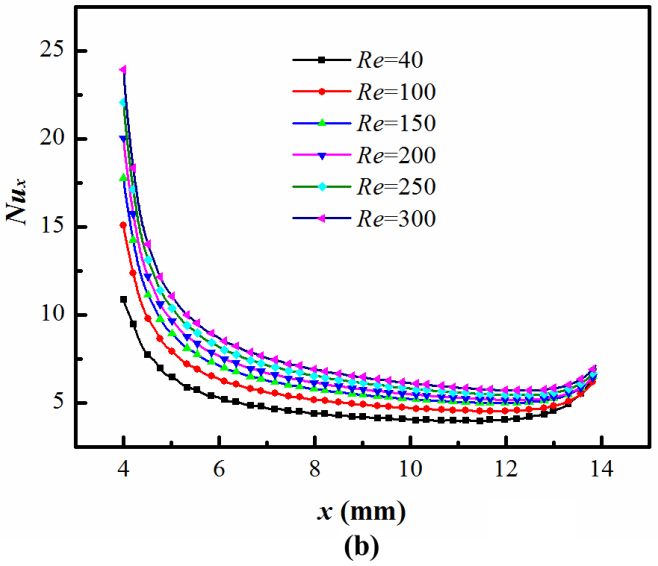

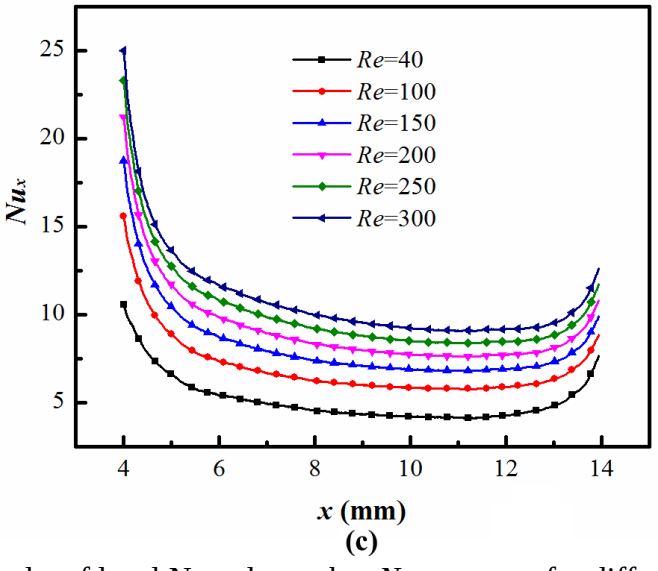

Fig. 21 Numerical results of local Nusselt number Nu_x versus x for different Re (a) C-MPF; (b) S-MPF; (c) D-MPF.